



NAVAL POSTGRADUATE SCHOOL

MONTEREY, CALIFORNIA

THESIS

**PREDICTIVE RELATIONSHIPS IN FRICTION STIR
PROCESSING OF NICKEL-ALUMINUM BRONZE**

by

William Patrick Pemberton

September 2005

Thesis Advisor:

Terry R. McNelley

Approved for public release; distribution is unlimited

THIS PAGE INTENTIONALLY LEFT BLANK

REPORT DOCUMENTATION PAGE			<i>Form Approved OMB No. 0704-0188</i>	
Public reporting burden for this collection of information is estimated to average 1 hour per response, including the time for reviewing instruction, searching existing data sources, gathering and maintaining the data needed, and completing and reviewing the collection of information. Send comments regarding this burden estimate or any other aspect of this collection of information, including suggestions for reducing this burden, to Washington headquarters Services, Directorate for Information Operations and Reports, 1215 Jefferson Davis Highway, Suite 1204, Arlington, VA 22202-4302, and to the Office of Management and Budget, Paperwork Reduction Project (0704-0188) Washington DC 20503.				
1. AGENCY USE ONLY (Leave blank)		2. REPORT DATE September 2005	3. REPORT TYPE AND DATES COVERED Master's Thesis	
4. TITLE AND SUBTITLE: Predictive Relationships in Friction Stir Processing of Nickel-Aluminum Bronze			5. FUNDING NUMBERS	
6. AUTHOR(S): W. Patrick Pemberton				
7. PERFORMING ORGANIZATION NAME(S) AND ADDRESS(ES) Naval Postgraduate School Monterey, CA 93943-5000			8. PERFORMING ORGANIZATION REPORT NUMBER	
9. SPONSORING /MONITORING AGENCY NAME(S) AND ADDRESS(ES) N/A			10. SPONSORING/MONITORING AGENCY REPORT NUMBER	
11. SUPPLEMENTARY NOTES The views expressed in this thesis are those of the author and do not reflect the official policy or position of the Department of Defense or the U.S. Government.				
12a. DISTRIBUTION / AVAILABILITY STATEMENT Approved for Public Release; Distribution is Unlimited			12b. DISTRIBUTION CODE	
13. ABSTRACT (maximum 200 words) Friction Stir Processing (FSP), a hot working materials processing technology, and various analytical and computational models for it are reviewed. A simulation is used to develop a new predictive relationship for power dissipated during FSP of Ni-Al bronze according to tool traversing velocity and rotational velocity. The model is then applied to empirical data and found to fit very well. Correlations between the cooling rate and material properties are examined. A relationship between cooling rate and ductility is found, and a predictive model is developed.				
14. SUBJECT TERMS friction stir processing, welding, nickel aluminum bronze, power, heat input, cooling rate, ductility, CTH, simulation, model			15. NUMBER OF PAGES 65	
			16. PRICE CODE	
17. SECURITY CLASSIFICATION OF REPORT Unclassified	18. SECURITY CLASSIFICATION OF THIS PAGE Unclassified	19. SECURITY CLASSIFICATION OF ABSTRACT Unclassified	20. LIMITATION OF ABSTRACT UL	

THIS PAGE INTENTIONALLY LEFT BLANK

Approved for public release; distribution is unlimited

**PREDICTIVE RELATIONSHIPS IN FRICTION STIR PROCESSING OF
NICKEL-ALUMINUM BRONZE**

W. Patrick Pemberton
Lieutenant, United States Navy
B.A., University of Texas, 1999

Submitted in partial fulfillment of the
requirements for the degree of

MASTER OF SCIENCE IN MECHANICAL ENGINEERING

from the

**NAVAL POSTGRADUATE SCHOOL
September 2005**

Author: William Patrick Pemberton

Approved by: Terry R. McNelley
Thesis Advisor

Anthony J. Healey
Chairman, Department of Mechanical and Astronautical
Engineering

THIS PAGE INTENTIONALLY LEFT BLANK

ABSTRACT

Friction Stir Processing (FSP), a hot working materials processing technology, and various analytical and computational models for it are reviewed. A simulation is used to develop a new predictive relationship for power dissipated during FSP of Ni-Al bronze according to tool traversing velocity and rotational velocity. The model is then applied to empirical data and found to fit very well. Correlations between the cooling rate and material properties are examined. A relationship between cooling rate and ductility is found, and a predictive model is developed.

THIS PAGE INTENTIONALLY LEFT BLANK

TABLE OF CONTENTS

I.	INTRODUCTION.....	1
A.	FRICTION STIR WELDING AND PROCESSING.....	1
B.	NICKEL-ALUMINUM BRONZE	4
C.	THE NEED FOR PREDICTIVE RELATIONSHIPS.....	5
II.	BACKGROUND	9
A.	EMPIRICAL RESULTS ARE NOT ENOUGH	9
B.	PREVIOUS MODELING EFFORTS.....	10
C.	CTH.....	11
III.	SIMULATION METHODOLOGY	15
A.	COMPUTER HARDWARE	15
B.	DEFINING THE TOOL.....	15
C.	DEFINING THE MESH	16
D.	VARIATION OF PARAMETERS.....	19
E.	QUANTITATIVE OUTPUT.....	20
IV.	RESULTS AND DISCUSSION	23
A.	POWER DEPENDENCE ON RPM.....	23
B.	POWER DEPENDENCE ON IPM	24
C.	POWER VARIATION WITH BOTH RPM AND IPM.....	26
D.	PLASTIC WORK VERSUS MECHANICAL WORK.....	28
E.	APPLICATION TO EMPIRICAL RESULTS FOR POWER.....	28
F.	EXTRAPOLATION OF HEAT INPUT	31
G.	EXTRAPOLATION OF COOLING RATE	32
H.	CORRELATION OF COOLING RATE TO DUCTILITY.....	33
I.	PREDICTION OF DUCTILITY.....	36
J.	CORRELATION TO OTHER MATERIAL PROPERTIES.....	37
V.	CONCLUSION	39
	APPENDIX A – EMPIRICAL DATA SETS.....	41
	APPENDIX B – SIMULATION RESULTS.....	43
	LIST OF REFERENCES.....	45
	INITIAL DISTRIBUTION LIST	49

THIS PAGE INTENTIONALLY LEFT BLANK

LIST OF FIGURES

Figure 1.	Friction Stir Welding diagram.	1
Figure 2.	FSP tool as simulated.	16
Figure 3.	Early simulation run with interference from lower mesh boundary.	17
Figure 4.	Mesh as used, with no adverse effect from lower boundary.	18
Figure 5.	Planar view of CTH finite volume mesh.	18
Figure 6.	Plot of simulated power converging to steady state value.	21
Figure 7.	Linear plot of power as a function of RPM.	23
Figure 8.	Logarithmic plot of power as a function of RPM.	24
Figure 9.	Linear plot of power as a function of IPM.	24
Figure 10.	Log-y plot of power as a function of IPM.	25
Figure 11.	Surface plot of power as a function of RPM and IPM.	26
Figure 12.	Surface plot of predicted power as a function of RPM and IPM.	27
Figure 13.	Surface plot of predicted power based on Rockwell empirical data.	30
Figure 14.	Heat Input as a function of RPM and IPM.	32
Figure 15.	Cooling Rate as a function of RPM and IPM.	33
Figure 16.	Ductility vs. cooling rate for all thirteen points.	34
Figure 17.	Averaged ductility versus cooling rate.	35
Figure 18.	Ductility as a function of RPM and IPM.	36
Figure 19.	Contour plot of ductility as a function of IPM and RPM.	37

THIS PAGE INTENTIONALLY LEFT BLANK

LIST OF TABLES

Table 1.	Johnson-Cook values for NAB.	13
Table 2.	Range of IPM values used.	19
Table 3.	Range of RPM values used.	20
Table 4.	Comparison of observed to predicted power.	29
Table 5.	Comparison of observed to predicted power.	30
Table 6.	Comparison of ductility to FSP inputs.....	34

THIS PAGE INTENTIONALLY LEFT BLANK

ACKNOWLEDGMENTS

The author would like to thank all of the people working on various parts of the DARPA friction stir process that provided help or input in some way: Dr. Stewart Silling of Sandia National Laboratory and Dr. Abe Askari of Boeing Corporation for help with the CTH software and assorted odd questions about the physics of friction stir; Dr. David Forrest and Ms. Mary Beth Marquardt for providing the computing facilities at Naval Surface Warfare Center Carderock and solving a great number of technical problems; Mr. Murray Mahoney of Rockwell Scientific Center for providing the necessary empirical data; Dr. Dan Nussbaum of NPS for instruction in the mathematics of curve fitting and statistical analysis; and Ms. Donna Burych of Naval Postgraduate School for much-needed on-campus computational support.

Special thanks to Dr. Terry McNelley, one of the most patient and dedicated people I've met throughout the Navy, for putting up with endless questions at all hours of the day.

Thanks to Dr. Keichiro Oishii and Dr. Alex Zhilyaev, for providing insight during the long process of finding trends in the data.

And of course, the most thanks to my wife Shanda, who has always supported me along the way.

THIS PAGE INTENTIONALLY LEFT BLANK

I. INTRODUCTION

A. FRICTION STIR WELDING AND PROCESSING

In 1991, a new joining technology called Friction Stir Welding (FSW) was patented by The Welding Institute [Ref. 1]. This new process held great promise as an alternative joining method in materials where conventional arc welding was difficult or simply impossible. Metallic pieces could be joined mechanically in solid state without the typical drawbacks encountered with other welding processes where melting and resolidification are the primary means of joining.

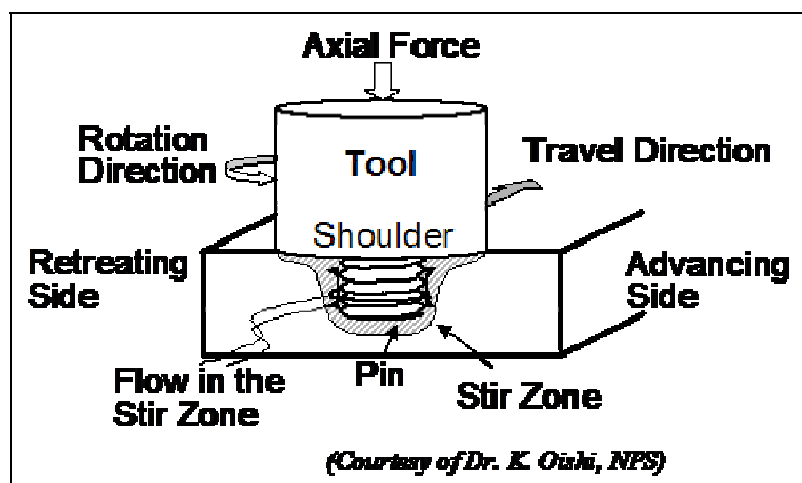


Figure 1. Friction Stir Welding diagram.

FSW is conceptually relatively simple. The FSW tool consists of a short metallic pin supported by a shoulder of greater diameter, as shown in Figure 1. Various pin designs have been developed, with different types of threads and other features designed to promote mixing of the material. The shoulder's main function is to provide an upper boundary during FSW to prevent material from being extruded out of the joint, but it may also have features such as scrolls or other shapes to promote mixing during FSW [Ref 2]. The tool is generally made of a material with a high hardness and melting temperature [Ref 1]. Tool steels are often used with Aluminum alloys, and refractory Tungsten-based alloys or Cubic Boron Nitride (CBN) ceramic materials are employed in FSW of higher melting metals [Ref 3].

The tool is rotated at high RPM and pressed into the components to be joined. As the tool comes into contact with the work piece, frictional heating between them causes thermal softening in the work piece metal. The pin is pushed all the way into the work pieces until the shoulder comes in contact with their upper surface, and then traversed laterally along the weld line [Ref 2].

The metal from both sides of the work piece is physically “stirred” together, from which the name of the process is derived. The rotation of the pin mixes the base materials together, physically deforming and adiabatically heating them [Ref 2]. But while high temperatures on the order of $0.9 T_M$ are observed, melting never appears to occur [Refs 1,4-7].

From this observation, it can be said that the process appears to reach equilibrium between strain hardening and thermal softening. As the material of the work pieces hardens during deformation more energy is required to continue to deform; but this raises the temperature and induces thermal softening, returning the process to equilibrium. Conversely, as thermal softening reduces the energy required to deform the material, temperature goes down and thermal softening is decreased, again returning the process to equilibrium. In other processes where metal is deformed at ordinary temperatures, such as extrusion or rolling, the heat generation from deformation is insufficient to provide for relaxation of stresses in the microstructure, and cracking or other failures will ultimately occur with continued deformation. But the strain rate of FSW is high enough that heat generated provides enough thermal softening to accommodate whatever strain hardening is taking place.

The positive attributes of FSW go well beyond the ability to make a physical bond between two pieces of metal. Within the stir zone where the material is mechanically deformed and mixed together and the high strain rate and high degree of plastic deformation results in a very refined, equiaxed grain structure [Ref 4-6]. In many alloys this translates into a weld zone with higher strength and, possibly, higher ductility than the original base metal microstructure. The relatively low heat input of the process reduces negative effects on microstructures outside the stir zone, within the heat affected zone. Environmentally, the process is very acceptable since it requires no shield gases,

fillers, or fluxes as with some arc welding processes, it creates little or no industrial waste, and is relatively more energy efficient in comparison to other welding technologies that may be used for the same applications.

Because of these characteristics, FSW has been proven capable of welding alloys and work pieces previously thought difficult to weld. As an example, high strength aluminum alloys used in aircraft construction have precisely controlled grain structures and temper states in order to achieve specific strengths and ductilities through solid solution strengthening or precipitation hardening. Traditional welding processes are often unuseable because they ruin these properties, and thus rivets or other mechanical joining methods are necessary [Ref 8]. But FSW tests of these materials have shown that it is an acceptable alternative [Ref 4]. Along with improvements in overall structural strength, the reduction in rivets and lap joints may result in a significant decrease of weight in the final aircraft. However, fixtures are necessary in order to constrain the forces necessary to accomplish FSW and this will limit some applications of the process.

Friction Stir Processing (FSP) seizes upon these beneficial characteristics of FSW and employs them in a different manner. Rather than joining two work pieces, the friction stir apparatus is used to process a single monolithic work piece [Ref 9,10]. The surface or part of a surface of the work piece is processed, resulting in a region of increased strength and ductility through grain refinement. This change in the local microstructure results allows the possibility of improving material properties in a work piece as desired, such as in places where fasteners will be attached [Ref 2].

Cast components in particular benefit from FSP. Castings are typified by very coarse grain structures, often encumbered by dendritic or needle-like second phases which promote fracture growth and propagation. When the components are very large and cooling times are very long, porosity and other defects also become common. Thus, the casting usually suffers from very low ductility and poor strength [Ref 2]. Grain refinement during FSP replaces the cast microstructure with a refined, equiaxed wrought microstructure [Ref 10]. Defects such as porosity and cracks are replaced with continuous work piece metal. FSP allows the possibility of combining the ease of manufacturing cast components with the material properties of wrought alloys.

B. NICKEL-ALUMINUM BRONZE

The US Navy is particularly interested in applying FSP to the manufacturing of Nickel-Aluminum Bronze (NAB) propellers. NAB is a commonly used alloy for propellers because of its useful combination of strength, toughness, and corrosion resistance. NAB is a copper based alloy, with additions of Nickel, Aluminum, Iron, and Manganese [Ref 11].

While NAB may be better suited than other materials in an as-cast state for use as a propeller material, it still suffers the drawbacks typical of castings. The large size of naval propeller castings exacerbates these characteristics by necessitating very long cooling times and thus low cooling rates [Ref 12]. This results in a rather coarse grain size. Porosity is also commonly exhibited as the low cooling rate allows entrapped gases to diffuse out of solidifying material and accumulate in pockets throughout the casting. These microstructural characteristics will also vary throughout the propeller with section size. Thinner sections such as the trailing edge or tip of a propeller blade will have higher cooling rates than the leading edge or main body of a propeller; thus, their microstructure will evolve differently, along with increased residual stresses [Ref 13].

Currently, these problems are rectified through post-casting processing techniques that are time consuming and only partially address the material property issues [Ref 14]. Heat treatments are used to reduce some of the residual stresses and increase strength, but this decreases an already low ductility. As the casting is machined into shape, porosity is repaired as it is encountered. The machining is stopped, the open fissure in the casting is filled manually via arc welding, and then machining continues. This is of course very tedious and may require many months to complete. The final product may still have undetected porosity just below the surface, and the welding may have created yet more unwanted microstructural effects and residual stresses [Ref 14]. In short, it is an expensive, inefficient, labor-intensive process that requires a relatively long time to produce a propeller which may still not meet design criteria.

It is possible that FSP of the casting could mitigate the need for both the heat treatment and the manual welding repair of porosity, and also address the issues which they do not. Suppose the propeller section were subjected to FSP prior to machining.

The cast material would be left with an outer layer of wrought NAB with higher strength, higher ductility, no porosity or cracks, and perhaps only minor residual stresses. Machining would be much quicker, without the need for frequent stops for welding repair. The high strength outer layer would lend the finished propeller a much higher resistance to wear and damage, resulting in a longer service life and fewer repairs.

C. THE NEED FOR PREDICTIVE RELATIONSHIPS

While general laboratory results have shown great promise, a significant issue has persistently prevented rapid adoption of FSP in propeller manufacturing. No predictive relationships or models exist for FSW or FSP as they do in traditional welding and processing technologies. All development thus far has relied on Edisonian experimental techniques, where various combinations of traversing speed and RPM are applied to test cases until an acceptable result is found. This is a plausible approach with small sections of aluminum that are easily procured.

Because of their size, the propeller castings themselves take a great deal of time and effort to produce, and a trial and error engineering approach is not feasible. Additionally, while it is possible to modify the multi-axis CNC machines used to finish the propellers to support FSP, the cost is not insignificant. Various laboratories and institutions have rigorously tested small sections of NAB plate, but the results have not conclusively led to a prediction of which combinations of RPM and velocity will lead to which combinations of properties. Some combinations produce excellent improvements in material properties, but some produce only marginal improvements, or even cause failure due to cracking or other defects. Without a predictive relationship, it is difficult to justify blind investment in the technology.

In conventional arc welding technologies, there are fairly robust prediction models for material properties. These prediction models are driven by equations derived from the basic equation for power dissipated in the welding process:

$$Q_H(\text{kW}) = \eta VI \quad (1)$$

The effective power dissipated in the weld (Q_H) is equal a thermal efficiency coefficient (η) times the voltage (V) times the current (I) [Ref 8]. Power is easily understood because it is linearly proportional to both voltage and current.

Next, the heat input (H) may be defined as:

$$H(\text{kJ/cm}) = \frac{Q_H}{v} \quad (2)$$

Heat input is proportional to the effective power dissipated, and inversely proportional to the velocity of the heat source [Ref 8]. Here, units of kJ/cm will be used; but in order to adhere to FSW conventions, velocity itself will be expressed in terms of inches per minute (IPM).

Cooling rate can be expressed in several different ways, but for the scope and intent of this paper, the Rosenthal thin plate, three dimensional cooling rate solution will be used:

$$\left(\frac{dT}{dt}\right)_x = \frac{2\pi k(T-T_0)^2}{H} \quad (3)$$

This equation is an analytical heat transfer solution based on conduction, which therefore makes it valid only outside of the weld pool, where no convection is taking place [Ref 8]. It gives the instantaneous cooling rate at a distance x behind the heat source where $T \leq T_M$, where T_M is the melting temperature. The cooling rate is proportional to the thermal conductivity of the material (k), the square of the temperature difference between the instantaneous temperature (T) and the ambient temperature (T_0), and inversely proportional to the heat input (H). This implies that cooling rate is also proportional to the velocity of the heat source (IPM), and inversely proportional to the effective power (Q), or

$$\left(\frac{dT}{dt}\right)_x = \frac{2\pi k(T-T_0)^2(\text{IPM})}{Q_H} \quad (4)$$

Since it is generally understood how most common alloys react to varying heat input or cooling rate, these welding or processing parameters can be manipulated in order to produce the desired material properties. For instance, steel alloys undergo a solid state

transformation as they cool from the melting point at the weld pool boundary down to the ambient temperature of the work piece. The resultant microstructure of the weld is thus strongly dependent on cooling rate. In order to prevent a martensitic microstructure which may be too hard and crack-prone relative to the rest of the work piece, the processing parameters can be modified to ensure a low cooling rate. The welder has several choices: he may increase power, reduce the velocity of the heat source, or impose some kind of preheating treatment of the work piece to reduce the temperature gradient throughout [Ref 8]. At any rate, the equations above are relatively simple and easy to apply, so long as the reaction of the base material is well understood.

Analysis of FSP has yielded no such simple solutions. Replacing voltage, current, and velocity, FSP has two underlying processing parameters: rotational velocity (RPM) and traversing velocity (IPM). Mechanical power input into the process is quantifiable by measuring torque and force in the traversing direction, but no obvious relationship between it and the processing parameters has yet been identified.

It has also not been clear what the relationship between that mechanical input energy and the final material properties means, if anything. In arc welding, the manner and rate at which the base material melts and resolidifies is central to the entire process. It is therefore relatively easy to draw a correlation between energy expended and the final material properties. In FSP on the other hand, both mechanical deformation and heat input are at work in defining the final microstructure, and no melting or resolidification takes place. It has not previously been shown that material properties can be correlated to power dissipated in a straightforward manner, as they are for arc welding.

In order to rectify these issues, this paper proposes a predictive relationship between RPM, IPM, and power, and explores the implied solutions for heat input and cooling rate. Additionally, correlations between these solutions and material properties in NAB are examined.

THIS PAGE INTENTIONALLY LEFT BLANK

II. BACKGROUND

A. EMPIRICAL RESULTS ARE NOT ENOUGH

While FSW and FSP have seen increasing use since the early 1990's, empirical results themselves have not lent enough insight towards obvious predictive relationships. As stated previously, most of the development has relied on Edisonian techniques, involving a search for combinations that work with the given work piece material. No methodical studies have been completed where IPM and RPM are varied with the intent of determining a relationship to power dissipation. Indeed, the FSP power results available for this paper are actually a byproduct of producing plates for material testing and microscopic analysis, rather than power prediction and correlation in of itself.

The data that is available has a high degree of variance, even for the same RPM and IPM combinations. The most complete data set available for NAB at this time consists of thirteen different plates subjected to FSP at Rockwell Scientific [Appendix A]. Among this set, plate thickness varies from 0.75 inches to 1.5 inches, and tool shoulder diameter varies from 1.01 inches to 1.125 inches. Only seven of these data points share a common shoulder width and plate thickness, and that number is further reduced to six since one combination of RPM and IPM is repeated.

A brief survey of the data reveals the obvious. By itself, there simply is not enough of it available to deduce a predictive relationship for power. The size of the set makes it difficult to identify outliers, and the variance of power and material properties with combinations of the same RPM and IPM alone add further confusion to the mix.

A methodical experiment could be envisioned that involves FSP of many test plates, with homogenous controlled conditions and a range of IPM and RPM values. Since its apparent that power and material properties can vary substantially for some IPM and RPM combinations, each combination would need to be run on a number of plates in order for an average power and average material properties to be determined.

However, substantial time and effort would be involved in this approach. Fortunately, computer modeling offers a more efficient approach. While the complexity of FSP ensures that no single simulation or set of assumptions is likely to ever fully

describe it, the simulations available can shed sufficient insight for numerical models to be derived and applied to the empirical data available.

B. PREVIOUS MODELING EFFORTS

Previous modeling efforts have focused primarily on understanding flow around the tool, with quantitative analysis as a secondary interest. The majority have been more concerned with analysis of how power is generated, rather than quantitatively or statistically predicting how much power is dissipated.

The simplest of these models assume that all heat is generated at the tool surface by sliding friction, and attempt to predict the heat conducted away from the stir zone independent of material motion. Chao and Qi developed one such model by iteratively tuning a heat transfer model to match empirical results. Using Coulomb's law to estimate the frictional force at the interface, they determined that the majority of heat generated is dissipated through the work piece rather than the tool [Ref 15,16]. Russell and Shercliff predicted the amount of frictional heat generation based on material properties at elevated temperature, and then combined it with Rosenthal's thin plate solution to model the heat dissipation [Ref 17]. Frigaard *et al.* set up a three dimensional heat dissipation model where the heat flux from the surface of the pin tool and shoulder is controlled. Heat flux from each element was adjusted until the predicted temperatures correlated with measured temperatures, and did not exceed expected maximums [Ref 18].

Schmidt *et al.* examined the assumption of sliding friction at the tool interface through analytical models for heat generation during FSW. They generated analytical solutions for heat generated using sliding friction and "sticking" friction, where the material adheres to the pin tool as a fluid might. By comparing the analytical predictions to laboratory tests they found that the sticking friction model is more accurate, and thus proposed that the sticking contact condition exists during FSW [Ref 19]. Colegrove and Shercliff used FLUENT, a two dimensional finite volume code, to explore the same question. Models for both sliding and sticking conditions were developed, and the flow around the tool was found to be substantially different with each assumption [Ref 20].

All of the models mentioned thus far assume only frictional heating of the material. When alloys are plastically deformed during a hot working process, the material is adiabatically heated. Arbegast observed that the microstructure within the stir zone resembled those produced by extrusion, and thus developed a model that incorporated heat generation from both friction at the tool interface and plastic deformation [Ref 21]. Bendzsak *et al.* used a fluid dynamics approach to model the heat dissipated using viscous flow rather than friction [Ref 22].

Laying the groundwork for this paper, Askari and Silling used the finite volume hydrocode CTH to model FSW and FSP. The simulation allows for quantitative analysis of the entire process or mesh element by mesh element, and flow visualization through graphical output [Ref 23].

Jamison used Askari and Silling's CTH model to develop a power prediction model based on simulation results [Ref 24]. By varying IPM between 1 and 20, and varying RPM between 50 and 5000, he determined that power dissipated during FSP of NAB follows a power law relationship to RPM and IPM:

$$Q(\text{kW}) = A \cdot \text{RPM}^b \cdot \text{IPM}^c \quad (5)$$

However, this predictive relationship cannot apply as IPM goes to zero at constant RPM because it predicts that power will go to zero. Engineering intuition says that this is not the case; indeed, during FSP the tool is plunged and held stationary until the work piece temperature rises and the material softens. This paper explores what happens as IPM approaches zero, and determines whether equation (5) is an appropriate fit.

C. CTH

CTH is a general purpose, finite volume model hydrocode that was originally written to simulate deformation during high speed impact and penetration. It is used in the simulation of large deformations of solid materials, and allows the user to choose from a selection of viscoplastic deformation prediction models. It uses a fixed Eulerian mesh, and thus models deformation by predicting how material will move from element to element. CTH alternates between solving the equations of state for continuity and momentum balance in each element, and then solves the energy balance equation of state

by solving for both convection and diffusion. It then predicts the change in temperature throughout the mesh by using the results of the energy balance equation of state and the heat generation in each element due to plastic deformation [Ref 25].

Because of its unique ability to model viscoplastic deformation in solids, CTH possesses an inherent advantage over the simulation methods used previously to model FSP. Finite element codes such as those used to model the sliding friction models are adept at simulating solid mechanics and elastic deformation between connected mesh nodes, but lose fidelity as the degree of plastic deformation increases. In the case of FSP where sticking friction is assumed, it is doubtful that the relationship predicted between mesh nodes wrapped around the pin tool at high RPM's are meaningful.

On the other hand, conventional finite volume models using fluid mechanics principles are better able to impose the sticking friction condition, but do not accurately reflect the reaction of the solid work piece to the movement of the pin tool. While material movement within the stir zone resembles fluid behavior, there is a distance away from the surface of the tool where the solid material resists shear deformation at equilibrium and elastically deforms, unlike a fluid.

CTH is able to overcome these issues by taking into account changes in material properties of NAB based on temperature and strain rate. It can thus model the NAB with varying resistance to deformation throughout the mesh. As modified by Askari and Silling, CTH uses the Johnson-Cook plasticity model to predict deformation during FSP [Ref 26, 27]. Their Johnson-Cook model incorporates predictions for strain hardening, thermal softening, and strain rate sensitivity, as in equations 6-8 (courtesy of Askari, Boeing, and Silling, Sandia National Laboratory):

$$g(\varepsilon^p) = \begin{cases} \sigma_o \left(1 + \frac{\varepsilon^p}{\varepsilon_o^p}\right)^{1/n} & \text{if } \varepsilon^p < \varepsilon_{cut}^p \\ \sigma_o \left(1 + \frac{\varepsilon_{cut}^p}{\varepsilon_o^p}\right)^{1/n} & \text{if } \varepsilon^p > \varepsilon_{cut}^p \end{cases} \quad (6)$$

$$\Theta(T) = \begin{cases} c_o + c_1 T + c_2 T^2 + c_3 T^3 + c_4 T^4 + c_5 T^5 & \text{if } T < T_{cut} \\ \Theta(T_{cut}) - \frac{(T - T_{cut})}{(T_{melt} - T_{cut})} & \text{if } T \geq T_{cut} \end{cases} \quad (7)$$

$$\sigma_{ys} = (A + B\varepsilon^{pN}) \left(1 + C \ln(\max(0.002, \dot{\varepsilon}^p))\right) \Theta(T) \quad (8)$$

Symbol	Name	NAB value
ε_o^p	Plastic strain reference	0.002
ε_{cut}^p	Plastic strain cutoff	0.46
σ_o	Reference stress	8.44×10^8 dyne/cm ²
n	Sensitivity factor	2.363
c_0	Temperature coefficient 0	1.0414
c_1	Temperature coefficient 1	-1.7144×10^{-3}
c_2	Temperature coefficient 2	1.1361×10^{-5}
c_3	Temperature coefficient 3	-3.6926×10^{-8}
c_4	Temperature coefficient 4	4.0437×10^{-11}
c_5	Temperature coefficient 5	-1.3749×10^{-14}
Tcut	Cutoff Temperature	800°C
Tmelt	Melting Temperature	1060°C
$d\varepsilon_o^p/dt$	Reference plastic strain rate	1 s ⁻¹
m	$= \partial \sigma / \partial (\dot{\varepsilon}^p)$	1/116

Table 1. Johnson-Cook values for NAB.

In addition to more accurately modeling the mechanical behavior of NAB at varying temperatures, CTH also takes into account heat generated due to plastic deformation. Power dissipated in this manner is calculated by numerically integrating the product of the stress, strain rate, and finite volume element size over the whole volume of the mesh, as in equation (9):

$$Q_H (\text{kW}) = \int_V \sigma \dot{\varepsilon} dV \quad (9)$$

Combining these characteristics allows CTH to generate more realistic simulations of FSP. The sticking friction assumption can be used, since adiabatic heating from equation (9) provides the temperature increase near the pin tool to cause thermal softening according to equation (7). Near the pin tool where the material has the least resistance to shear deformation due to this effect, CTH can simulate its motion in a fluid like manner. Away from the tool surface where the temperature is lower, CTH can simulate it resisting shear deformation elastically rather than continuing to deform as a fluid might [Ref 23].

As with other finite volume models, CTH functions by imposing boundary conditions on the mesh, and then iteratively balancing equations of state throughout. For FSP, the radial velocity (RPM) and traversing rate (IPM) are imposed at the tool surface, and the reaction of the material in the mesh is then calculated.

III. SIMULATION METHODOLOGY

A. COMPUTER HARDWARE

All simulations were run on an SGI Origin 3000 server, provided by Naval Surface Warfare Center Carderock, Maryland. The simulation required approximately 2GB of physical memory, and an additional 3.5GB of virtual memory. Using the full mesh size available in CTH, completing each simulation required roughly 72 hours of run time. Three simulations could be run simultaneously.

The post-processed results were then stored locally on a Linux-based server. Analysis was done on both the Linux server and Windows based PC's using MATLAB and Microsoft Excel.

B. DEFINING THE TOOL

For practical reasons, it was determined that the simulations should be based as much as possible on the tool and plate geometries in use for the bulk of the empirical experiments available. While CTH can simulate a large variety of tool shapes and any number of sizes, it would be most useful if the simulation results could be compared directly to laboratory results for similar conditions. The majority of the NAB FSW and FSP work completed to date by Rockwell Scientific has used a Densimet tool with a 0.50 inch pin length and a 1.01 inch shoulder diameter. The pin is the frustum of a cone and has a stepped spiral pattern on the cone surface in order to promote material flow in the z direction.

The tool was coded into the simulation based on the dimensions and specifications provided by Rockwell Scientific. Figure 2 is a rendering of the pin tool as simulated by CTH.



Figure 2. FSP tool as simulated.

C. DEFINING THE MESH

Although CTH itself is capable of modeling mesh grids in any of the common coordinate systems, the FSP version is limited to a rectangular mesh and rectilinear coordinate system. Additionally, this version has an upper limit on the number of mesh elements. Up to 151 elements may be used in the x and y directions, and up to 55 may be used in the z direction. CTH will also accommodate distorted elements, and different variable mesh size schemes.

CTH requires several different mesh zones to be defined. At the bottom of the mesh, a rigid steel back plane is set, akin to an anvil or machining table where a work piece may be secured. The back plane does not deform or move, but does conduct heat out of the work piece. The next mesh layer is the NAB work piece itself. The work piece material is fed into the work piece mesh in the x direction at a defined velocity (IPM), while the tool and back plane remain stationary. The top layer of the mesh is an air layer, which also conducts heat away from the work piece. Lastly, the pin tool and shoulder are defined and located within the middle of the mesh grid. No material flow is allowed from one zone to another, and only the work piece material deforms.

Creating a mesh requires balancing desired accuracy and practical computational limitations. Smaller mesh elements will increase the accuracy of the model, but will raise the amount of time and computational resources required. Conversely, large elements

will decrease the accuracy, but reduce the time and resources required. Distorted meshes allow a compromise of sorts, where small elements may be used where higher accuracy is required, and large elements may be used where low accuracy is acceptable.

In this experiment, the mesh size and element size were driven by several factors. The highest degree of accuracy in the mesh is obviously desired near the pin tool, where the gradients for temperature, stress, and material flow will be the highest. Outside of the stir zone where the only transport phenomenon expected is heat conduction, a larger mesh element will suffice.

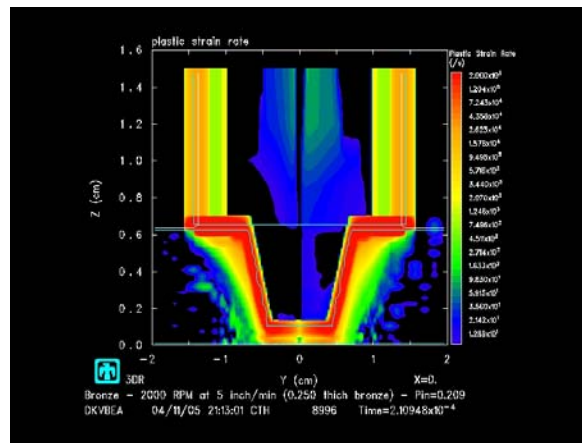


Figure 3. Early simulation run with interference from lower mesh boundary.

Earlier trial simulations revealed that if the tool tip is too close to the bottom of the work piece, the boundary conditions set at the bottom of the plate will interfere with material flow in the simulation. Figure 3 shows one of these early runs, and illustrates how material flow was adversely affected by the bottom of the mesh. Through trial and error, it was found that a distance of 0.25 inches was the minimum required clearance between the tool tip and the bottom of the work piece. Figure 4 is one of the later simulations with increased clearance, unhindered by the lower mesh boundary. Thus, with a 0.50 inch pin tool, a work piece thickness of 0.75 inches was necessary.

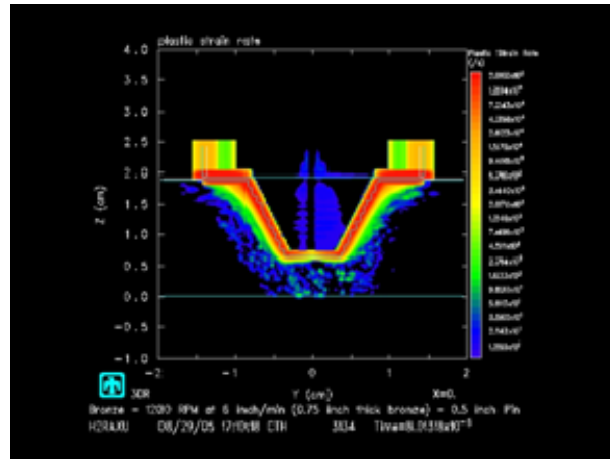


Figure 4. Mesh as used, with no adverse effect from lower boundary.

By minimizing the number of vertical elements in the air and backplane zones, and distorting them so that they increased progressively in size away from the work piece, it was possible to use very small elements within the work piece, ranging from 0.03cm to 0.05cm near the pin tool. A planar view of the final mesh is displayed in Figure 5.

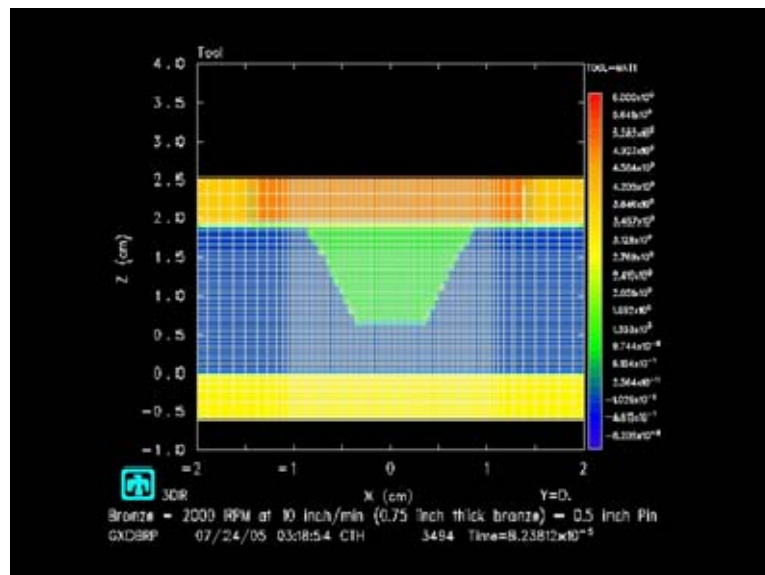


Figure 5. Planar view of CTH finite volume mesh.

D. VARIATION OF PARAMETERS

The primary processing parameters to be examined are rotational velocity (RPM) and traversing speed (IPM). For practical purposes, only RPM and IPM combinations considered within normal operating ranges are considered.

As previously discussed, the prediction model derived by Jamison fit the available simulation data rather well, but did not accurately portray what would happen as traversing rate goes to zero. Obviously, torque is still being applied, so power must be dissipated. But, the relationship $Q \propto \text{IPM}^n$ implies that power goes to zero as traversing rate goes to zero.

CTH will not allow the user to define a traversing speed of zero but it will allow arbitrarily slow rates to be used. In order to examine power dissipation as speed goes to zero, the IPM range was varied logarithmically across three decades, from 0.01 IPM to 10 IPM.

IPM Range	0.01	0.1	1	3	6	10
------------------	------	-----	---	---	---	----

Table 2. Range of IPM values used.

Rotational speed was varied between 600 and 2000 RPM, with values chosen to match those used in laboratory work. Low RPM values approaching zero were avoided for practical reasons. While the power dissipated by the pin tool moving laterally at zero RPM is most likely non-zero, in the real world this is most likely no longer a “stirring” process, and is probably more akin to physically gouging the work piece.

Traversing rates, on the other hand, will certainly approach or reach zero on a regular basis, at least during the initial and final steps of FSP. If nothing else, it is worthwhile to examine whether or not the equilibrium state between thermal softening and strain hardening continues to exist as the pin tool ceases to move laterally.

RPM Range	600	800	1000	1200	2000
-----------	-----	-----	------	------	------

Table 3. Range of RPM values used.

The end result of this variation of parameters is a set of thirty data points that span the useful range in both RPM and IPM dimensions, and provide enough data points for accurate curve fitting along each axis.

E. QUANTITATIVE OUTPUT

Each CTH simulation run generates a great deal of post-processed data, ranging from graphical output of data along planes within the mesh, to specific instantaneous and time history quantities for each element in the mesh.

For the purposes of this paper, however, we limit ourselves to discussing the data relevant to power dissipation. During each finite time step, CTH provides output to the user with several useful quantities for calculating the total power: the total moment balance for the mesh or total torque, and the total balance of forces in the x direction. When these quantities are combined with the known conditions of the simulation, rotational velocity and traversing rate, or RPM and IPM, the total mechanical power (Q_M) can be calculated as:

$$Q_M (\text{kW}) = T\omega + F_x v \simeq T(\text{RPM}) + F_x(\text{IPM}) \quad (9)$$

CTH also provides a direct calculation for the rate of plastic work done for each time step. This is equivalent to the rate at which heat work is done, or (Q_H):

$$Q_H = \int_V \sigma \dot{\epsilon} dV \quad (10)$$

The simulation is run until these values converge to a steady value, when it can be said to have reached “steady state,” which takes approximately 2000 to 3000 cycles. Figure 6 is a representative plot that illustrates how the power varies while the simulation

steadies itself. The work rate is then taken to be the average of the last 300 cycles at steady state. This provides a good estimate of power dissipated with an arbitrarily small standard error.

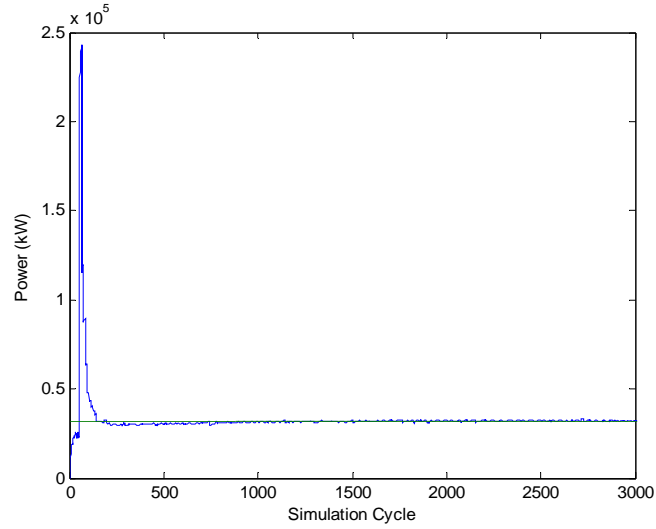


Figure 6. Plot of simulated power converging to steady state value.

THIS PAGE INTENTIONALLY LEFT BLANK

IV. RESULTS AND DISCUSSION

A. POWER DEPENDENCE ON RPM

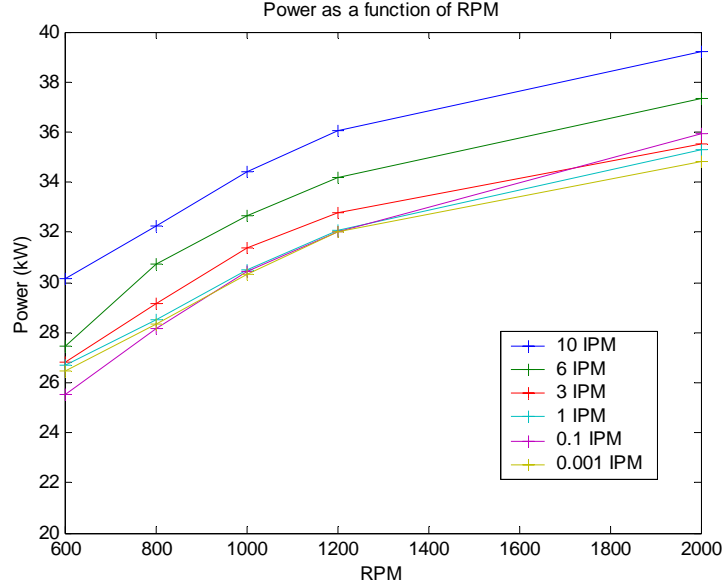


Figure 7. Linear plot of power as a function of RPM.

Figure 7 shows how power varied with RPM. Here, the lines in the scatterplot group the data according to constant IPM. Power appears to tend towards zero as RPM approaches zero. Power increases with RPM, but not linearly. The plot lines are concave down.

Again through trial and error, a power law is found to fit this data set very well. It satisfies both the shape and trends of the data, and is quantitatively a good fit. The results agree with the prediction proposed by Jamison, as they should since they cover a similar range of RPM [Ref 24]. Figure 8 displays the data again, but on a logarithmic scale along each axis, where a power law function will plot as a straight line.

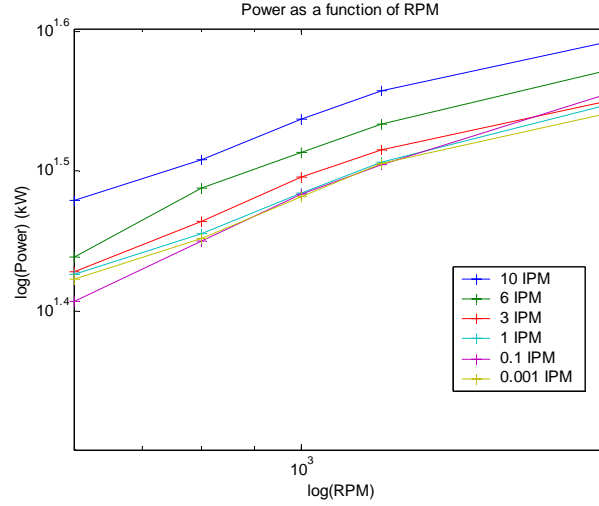


Figure 8. Logarithmic plot of power as a function of RPM.

Thus, power can be said to vary with RPM according to the following relationship:

$$Q_M (\text{kW}) = A \cdot \text{RPM}^b \quad (11)$$

B. POWER DEPENDENCE ON IPM

As expected, mechanical power did not approach zero as IPM tends to zero. Power appears instead to converge to a steady value as velocity decreases below one IPM. The scatterplot in Figure 9 displays the raw data from the simulation, grouped in lines according to constant RPM.

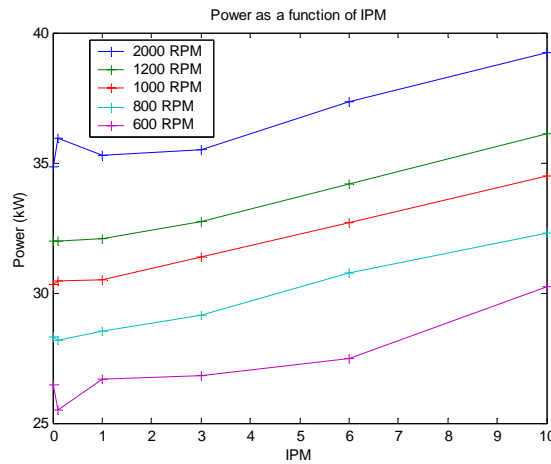


Figure 9. Linear plot of power as a function of IPM.

While the power law model provided a good fit for the data between one and ten IPM, its shortcomings are now obvious. Moreover, these data sets appear to be concave up at low IPM values; the power law prediction curve was concave down.

A new formulation is therefore required to accurately characterize the data set. Trial and error with different ordinary least squares (OLS) fitting methods revealed that an exponential fit will work well here. An exponential curve satisfies engineering intuition by converging to a constant value as IPM goes to zero. It also describes the upward concavity of the curve.

Figure 10 shows the data replotted with the velocity rescaled logarithmically on the y axis. Exponential curves will resemble straight lines when plotted on a log-y plot.

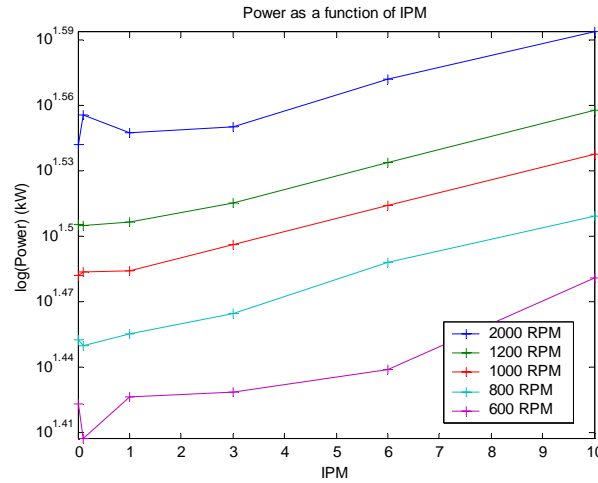


Figure 10. Log-y plot of power as a function of IPM.

Thus, power can then be said to vary with IPM according to the following relationship:

$$Q_M (\text{kW}) = A \cdot e^{(c \cdot \text{IPM})} \quad (12)$$

C. POWER VARIATION WITH BOTH RPM AND IPM

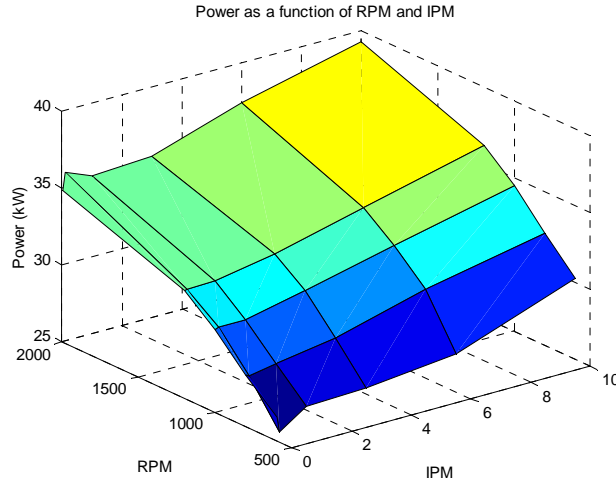


Figure 11. Surface plot of power as a function of RPM and IPM.

In Figure 11, a surface plot is shown to summarize all of the simulation power results, with IPM and RPM along the independent axes and mechanical power along the z axis. The raw data is available in Appendix B. As in the two-dimensional plots, it is qualitatively apparent that equations (11) and (12) are good predictions for power according to IPM and RPM individually. But a general equation that combines both input parameters is the objective.

The full equation can be found for the whole set of data using ordinary linear regression. Combining the two expressions above into a single equation yields the following result:

$$Q(kW) = A \cdot \text{RPM}^b e^{(c \cdot \text{IPM})} \quad (13)$$

This prediction model can be fitted to the data using normal linear regression techniques. The data set describes a system of thirty equations with three unknowns of the form shown in equation (14) below, which are the three coefficients in equation (13) above.

$$\begin{bmatrix} 1 & \log(\text{RPM}) & \text{IPM} \end{bmatrix} = \log(Q_M) \quad (14)$$

Solving this system in MATLAB gives us values for the coefficients that fit the model to the data in the OLS sense:

$$Q(\text{kW}) = 5.60 \cdot \text{RPM}^{0.242} e^{(0.013 \cdot \text{IPM})} \quad (15)$$

Figure 12 shows the prediction model within the same range as Figure 11. Comparison of the two illustrates that this prediction model is qualitatively a good fit for the data. It captures the relevant trends well, and appears to match the values very well.

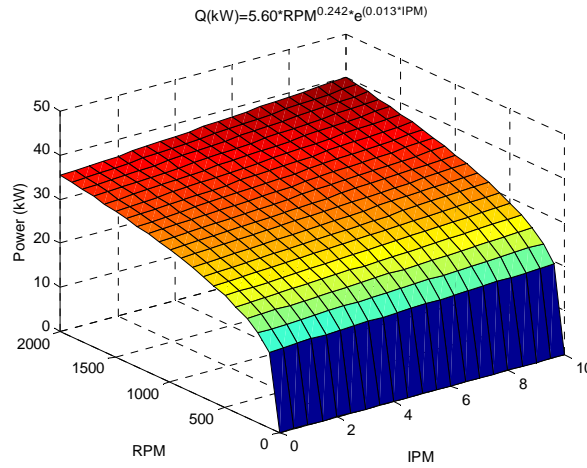


Figure 12. Surface plot of predicted power as a function of RPM and IPM.

Quantitatively, the prediction model is an excellent fit. The square of the Pearson product-moment coefficient (R^2) is an indicator of how much of the variation in one set of data is proportional to the variation in another [Ref 28]. It varies between zero and one, with higher values indicating greater degrees of correlation. Here, R^2 between the data and the prediction is 0.974. The standard error of the model is 0.11kW, and the coefficient of variation (CV) is 0.3%.

For quantitative comparison to the previous model, the data can be fit to an equation where $Q \propto \text{IPM}^n$. The regression is performed in the same manner:

$$\begin{aligned} [1 \quad \log(\text{RPM}) \quad \log(\text{IPM})] &= \log(Q) \\ \Rightarrow Q(\text{kW}) &= 5.86 \cdot \text{RPM}^{0.24} \text{IPM}^{0.014} \end{aligned}$$

In this case, R^2 decreases to 0.895. The standard error increases to 0.22kW, and the CV increases to 0.7%. Thus, equation (13) provides a superior fit for both qualitative and quantitative reasons.

D. PLASTIC WORK VERSUS MECHANICAL WORK

As with mechanical power, a plastic work rate was extracted from each simulation run. The plastic power dissipated was always 60% +/- 1% of the total mechanical power dissipated. Thus, the OLS fit to the data for plastic or effective power can be expressed simply as $Q_H = \eta Q_M$, where η in this case is a constant thermal efficiency of 0.60.

While the implications of a constant thermal efficiency are both interesting and useful, it must be acknowledged that empirical validation of this result is rather difficult. As discussed previously, the complexity of FSP makes measurement of thermal power dissipated inherently difficult with the best of equipment. It is possible that the real efficiency is not constant, and this result is caused by using the Johnson-Cooke plasticity model exclusively. That being said, a constant efficiency is not unbelievable either, and the possible variance within the useful window of IPM and RPM is most likely small.

E. APPLICATION TO EMPIRICAL RESULTS FOR POWER

Now that simulation data has lent enough insight to generate a suitable prediction model, the real test comes with trying to fit the model to available empirical data. In section I it was mentioned that only thirteen data points were available, and not enough exist along constant RPM or constant IPM lines to define a single variable function. However, since we are attempting to fit a bivariate model to a surface, it becomes advantageous that the thirteen points are randomly distributed across the RPM-IPM range.

Once again, an OLS regression fit was performed, but this time only the power data gathered by Rockwell Scientific was used. The result has different coefficients, but the model fits the data rather well:

$$Q_M (\text{kW}) = 0.077 \cdot \text{RPM}^{0.67} \cdot e^{(0.061 \cdot \text{IPM})} \quad (16)$$

The table below shows the difference between the observed power and the prediction model:

Rockwell 13 Point Fit			
<i>RPM</i>	<i>IPM</i>	<i>Observed (kW)</i>	<i>Predicted (kW)</i>
600	2	6.38	6.31
600	5	7.13	7.57
800	2	7.45	7.64
800	2	7.78	7.64
800	2	7.41	7.64
800	4	9.34	8.64
800	6	9.69	9.76
1000	2	9.77	8.88
1000	3	9.92	9.43
1000	3	8.81	9.43
1000	4	10.38	10.03
1200	2	9.60	10.03
1200	2	9.51	10.03

Table 4. Comparison of observed to predicted power.

Subjectively the model appears to fit the data well, and as with the simulation, captures what intuition says should happen as RPM and IPM increase or decrease. Qualitatively, R^2 is 0.861, the standard error is 0.52kW, and the CV is thus 5.9%. Consider the multiple data points in the above set, such as 800 RPM and 2 IPM. The variation amongst these repeated data points alone can be as high as 12%. For a model fitted to data with relatively high inherent variance, this is a very good fit.

It was mentioned previously that only seven of the thirteen data points use the exact same plate thickness and tool shoulder diameter. For completeness, those seven points are analyzed separately here. The OLS fit becomes:

$$Q_M (\text{kW}) = 0.065 \cdot \text{RPM}^{0.69} e^{(0.064 \cdot \text{IPM})} \quad (17)$$

Rockwell 7 Point Fit			
<i>RPM</i>	<i>IPM</i>	<i>Observed (kW)</i>	<i>Predicted (kW)</i>
600	2	6.38	6.27
600	5	7.13	7.59
800	2	7.78	7.65
800	2	7.41	7.65
800	4	9.34	8.69
1000	3	9.92	9.52
1200	2	9.60	10.13

Table 5. Comparison of observed to predicted power.

Quality of the fit improves somewhat, with R^2 increasing to 0.898, while the standard error increases to 0.26kW. This results in a CV of 3.2%, which is again less than the variation seen at the repeated data point in the set.

Comparison between this model and the simulation-derived model reveal several things about CTH. It over-predicts power, but under-predicts its dependence on IPM and RPM. The leading coefficients appear quite different, but this is only because of the difference in the intercept points in the logarithmically transformed data for the model. Figure 12 shows a surface plot of the empirically-derived prediction model. Visual comparison between it and Figure 11 shows that the lower observed power numbers and higher dependence on RPM and IPM result in a much lower leading coefficient, or intercept point.

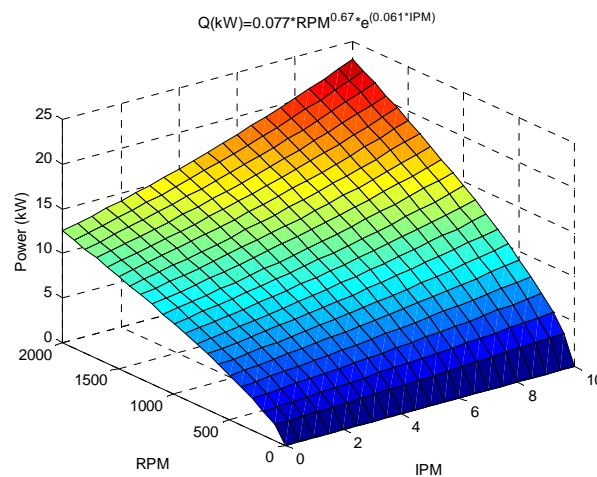


Figure 13. Surface plot of predicted power based on Rockwell empirical data.

For the remainder of the paper, the thirteen data point fit will be used to represent empirical results. While it can be argued that the seven point fit is better on several counts, the final equations vary little from one another, and the thirteen point fit is representative of a more generalized set.

F. EXTRAPOLATION OF HEAT INPUT

Power by itself is only the first part of the puzzle; the actual welding parameters that affect material properties are heat input and cooling rate. In section I, the general welding equations were discussed. Heat input is proportional to effective power, and inversely proportional to the velocity or IPM of the heat source.

$$H = \frac{\eta Q_M}{IPM} \quad (18)$$

In conventional arc welding these relationships are linearly proportional to power and velocity, but in FSP the relationship is more complex. Using the general equation for FSP power (13), heat input is therefore

$$H = \frac{Q_H}{IPM} = \frac{A \cdot RPM^b e^{(c \cdot IPM)}}{IPM} \quad (19)$$

With the simulation results, there is a quantitative result for thermal efficiency. But with the Rockwell results, there is no simple way to determine it. So, with a lack of insight from other means, it is assumed that thermal efficiency is constant. Thus, 60% is used for extrapolation purposes here, although if it were a different number the trend would remain the same, despite the changes in absolute value. Figure 14 illustrates a surface plot of heat input as a function of IPM and RPM.

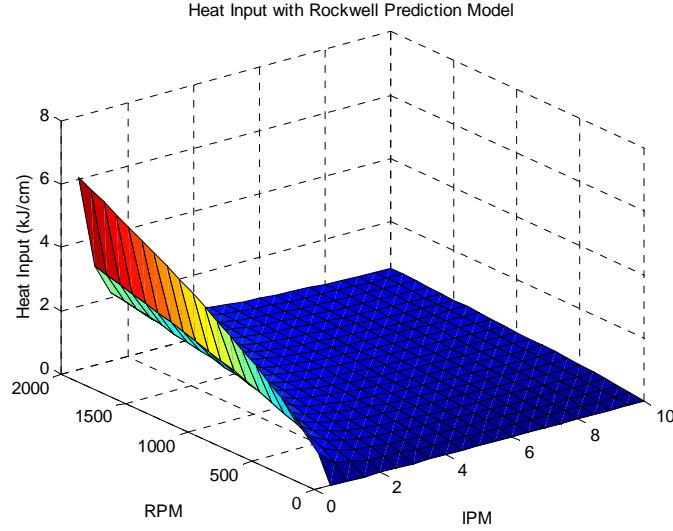


Figure 14. Heat Input as a function of RPM and IPM

Here, it is shown that heat input varies as one would expect. It increases with power and decreases with velocity. Although the relationships are complex, they follow general expectations in behavior.

G. EXTRAPOLATION OF COOLING RATE

Next, cooling rate is examined. Although the stir zone is a more complex feature than the weld pool in a conventional arc welding process, general heat transfer solutions should be valid outside of the stir zone where no material flow is taking place. Previous work by Vasquez and Pierce [Ref 29,30] suggest that since NAB ceases to flow easily below 800°C, this temperature could be used to define the outer edge of the stir zone where convection ceases and only conduction occurs.

The Rosenthal two-dimensional, thin plate cooling rate equation gives the instantaneous cooling rate at a point x behind the heat source:

$$\left(\frac{dT}{dt}\right)_x = \frac{2\pi k(T-T_0)^2}{H} \quad (20)$$

Using $T=800^\circ\text{C}$, and an ambient temperature of $T_0=20^\circ\text{C}$, the cooling rate is extrapolated and plotted in Figure 15 as a function of RPM and IPM.

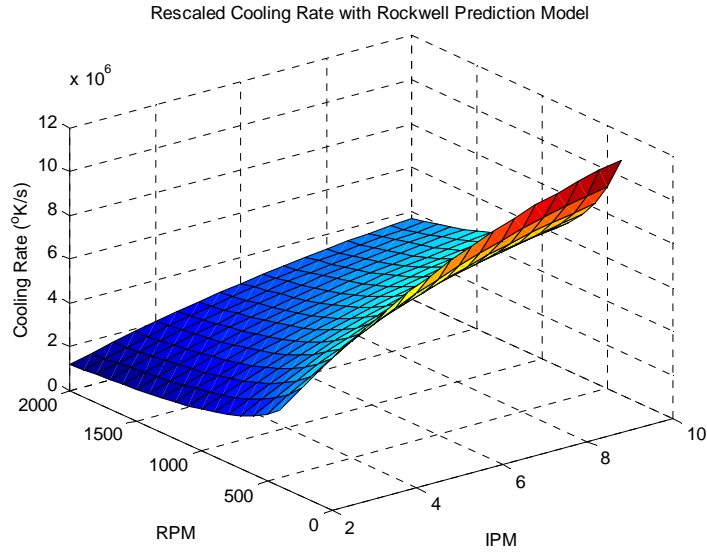


Figure 15. Cooling Rate as a function of RPM and IPM

As with heat input, the cooling rate performs as expected. It is proportional to velocity, and inversely proportional to power dissipated.

H. CORRELATION OF COOLING RATE TO DUCTILITY

In many welded metals, ductility is strongly affected by cooling rate. A low heat input, high cooling rate process can result in brittle transformation products such as martensite, and low ductility. Conversely, a high heat input, low cooling rate process allows sufficient energy and time for relaxation of residual stresses and other mechanisms that increase ductility, such as recrystallization. Speed and power in conventional welding processes are thus varied to obtain a desired degree of ductility [Ref 8].

Tensile tests of hot rolled NAB by McNelley and Oishi [Ref 31] have suggested that the ductility of NAB is similarly affected by cooling rate. However, no direct work has been done relating ductility in NAB to power in FSP because of the lack of understanding of how power is dissipated, and how it affects heat input and cooling rate.

Table 5 displays the observed values of mechanical power dissipated for each of the thirteen points, along with extrapolated values for heat input and cooling rate according to the equations previously discussed. Ductility for each sample is included in

the last column as percent elongation. Ductility was measured for each point at six different locations on the plate within the FSP using a tensile specimen with a diameter greater than the stir zone itself.

Rockwell 13 Point Fit					
<i>RPM</i>	<i>IPM</i>	<i>Observed Power (kW)</i>	<i>Heat Input (kJ/cm)</i>	<i>Cooling Rate ($^{\circ}\text{K/s}$)</i>	<i>Ductility</i>
600	2	6.38	45.24	62464	15.0
600	5	7.13	20.21	139825	10.9
800	2	7.45	52.82	53501	28.6
800	2	7.78	55.16	51232	12.1
800	2	7.41	52.49	53833	15.5
800	4	9.34	33.08	85412	15.9
800	6	9.69	22.89	123473	7.6
1000	2	9.77	69.26	40803	22.4
1000	3	9.92	46.86	60308	23.0
1000	3	8.81	41.62	67891	8.3
1000	4	10.38	36.79	76811	11.8
1200	2	9.60	68.01	41552	16.1
1200	2	9.51	67.39	41931	22.2

Table 6. Comparison of ductility to FSP inputs

When plotted, a relationship between ductility and cooling rate emerges. Figure 16 shows tensile elongation as a function of calculated cooling rate:

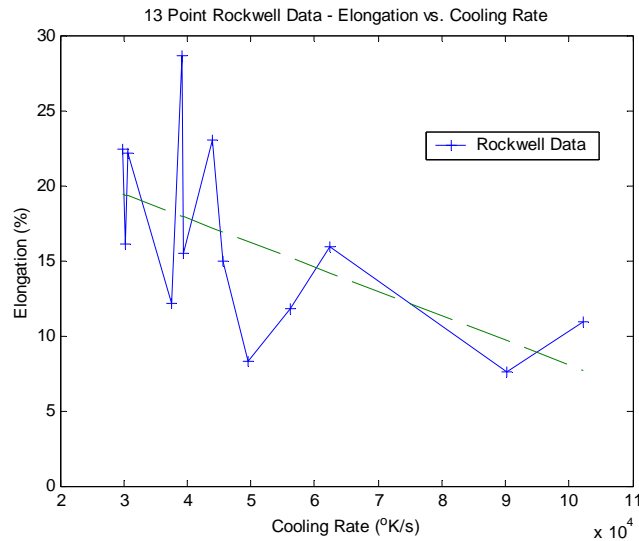


Figure 16. Ductility vs. cooling rate for all thirteen points.

While the trend is clear, it is also obvious that a great deal of scatter exists in the data, especially to the left. In this plot R^2 is 0.36, suggesting a weak correlation.

However, this picture can be improved. Empirical formulations are typically based on statistical data from many experiments using the same inputs, in order to produce meaningful results. Not only is this data set limited in size, but in order to get a truly clear correlation, each data point would ideally be repeated several times to find an average.

When fitting the power prediction model to the data, it was computationally beneficial that the thirteen points were randomly distributed over the RPM and IPM range. Now it becomes beneficial that several of the IPM and RPM combinations are repeated. Note the repeated points in Table 5. Taking the average of those data points for cooling rate and ductility and replacing them with a single point removes several of the outliers and greatly reduces the amount of unexplained variation in the set.

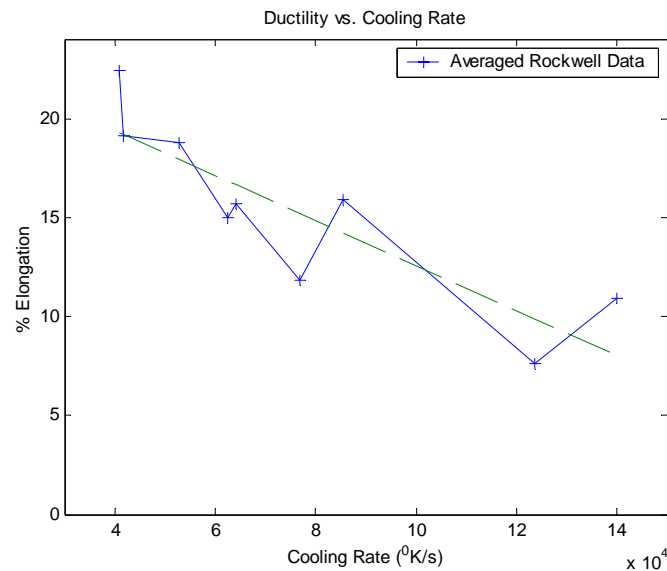


Figure 17. Averaged ductility versus cooling rate.

Figure 17 displays the averaged data. The correlation is now much stronger, with R^2 increasing to 0.75.

I. PREDICTION OF DUCTILITY

Two important pieces of the puzzle have now been identified. Based on empirical results, and using insight from simulation data, a power prediction model has been identified. It brings with it associated expressions for heat input and cooling rate. A strong correlation between ductility and the observed power dissipated has also been found. Putting these two parts together gives rise to a prediction model for ductility based on RPM and IPM.

Figure 18 shows a prediction model based on the linear relationship between ductility and cooling rate found in the previous section, and the linear relationship between cooling rate and ductility shown in Figure 17.

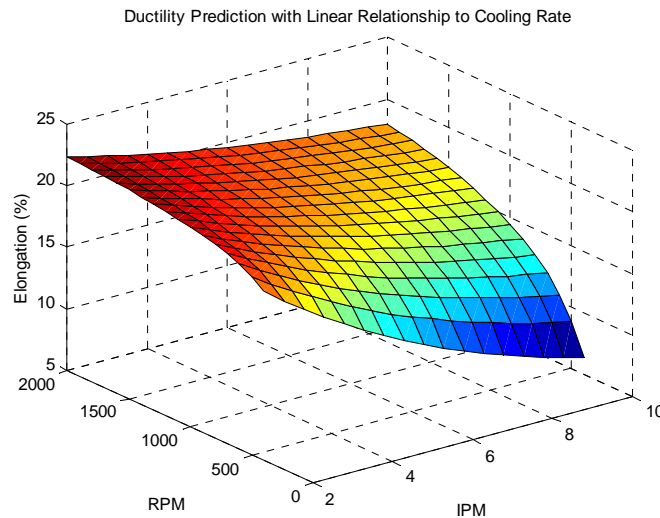


Figure 18. Ductility as a function of RPM and IPM

The model predicts low ductility with higher speeds and lower power input, and higher ductility with lower speeds and higher power input.

Figure 18 is presented as a surface plot for continuity. But a contour plot of the same data is perhaps more interesting and practically useful.

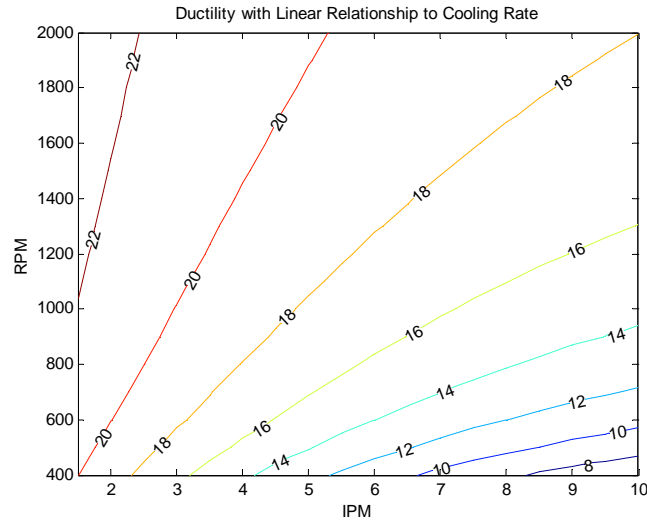


Figure 19. Contour plot of ductility as a function of IPM and RPM.

With the prediction model represented in this manner, the practical application of the prediction model becomes inherently obvious. It is easy to envision a simple ductility map such as this being used during application of FSP in NAB.

J. CORRELATION TO OTHER MATERIAL PROPERTIES

The Rockwell data set also contained values for yield strength and ultimate tensile strength for each data point. Comparison of these values to observed and predicted values for heat input and cooling rate found little or no correlation. There was also no clear trend according to IPM and RPM, or variations in x-direction force or torque.

This implies that these material properties are determined by conditions other than those analyzed here. However, it must be noted that the overall variation in yield strength and ultimate tensile strength is far less than that found in ductility. Yield strength varies no more than 10% from plate to plate, while ductility can jump from 28% elongation to 7% elongation. It must also be said that neither yield strength nor ultimate tensile strength has been an issue in the FSP samples to date, as the lowest experimental numbers for each is still a great improvement over as-cast NAB. Ductility has caused the most concern due to its previously unexplainable high variance.

THIS PAGE INTENTIONALLY LEFT BLANK

V. CONCLUSION

In summary, several conclusions can be drawn from this work. Mechanical power dissipated is proportional to a power law function of RPM and an exponential function of IPM (equation 13). This formulation brings with it expressions for heat input and cooling rate. Ductility is inversely proportional to cooling rate, and a prediction model for ductility in FSP of NAB can be generated combining the power prediction model with observed empirical results.

Future laboratory work should be directed towards refining the model through statistical insight. Future production work using FSP should take into account the effects of cooling rate on ductility in NAB, and perhaps other metals. The ductility map in Figure 19 should be considered as a prototypical FSW/FSP engineering tool for avoiding combinations of RPM and IPM that may generate low ductility in a finished product.

THIS PAGE INTENTIONALLY LEFT BLANK

APPENDIX A – EMPIRICAL DATA SETS

Rockwell Scientific FSP Results – 13 Point Set							
RPM	IPM	Torque (ft-lbs)	x-dir. Force (lbs)	Power (kW)	Yield Strength (ksi)	Ultimate Tensile Strength (ksi)	Ductility (% Elongation)
600	2	74.9	850	6.38	74.22	119.4	15
600	5	83.4	2640	7.13	73.20	113.77	10.9
800	2	65.6	570	7.45	64.53	109.68	28.6
800	2	68.5	740	7.78	72.15	114.2	12.11
800	2	65.2	440	7.41	73.68	117.8	15.5
800	4	82.1	1590	9.34	73.39	118.8	15.92
800	6	85.0	3000	9.69	66.4	90.25	7.63
1000	2	68.8	1180	9.77	68.16	109.67	22.4
1000	3	69.8	1390	9.92	72.27	113.93	23.02
1000	3	62.0	1310	8.81	70.16	100.18	8.27
1000	4	73.0	2420	10.38	75.37	109.8	11.8
1200	2	56.3	1170	9.60	75.01	115.47	16.07
1200	2	55.8	730	9.51	68.34	112.68	22.15

Rockwell Scientific FSP Results – 7 Point Set							
RPM	IPM	Torque (ft-lbs)	x-dir. Force (lbs)	Power (kW)	Yield Strength (ksi)	Ultimate Tensile Strength (ksi)	Ductility (% Elongation)
600	2	74.9	850	6.38	74.22	119.4	15
600	5	83.4	2640	7.13	73.20	113.77	10.9
800	2	68.5	740	7.78	72.15	114.2	12.11
800	2	65.2	440	7.41	73.68	117.8	15.5
800	4	82.1	1590	9.34	73.39	118.8	15.92
1000	3	69.8	1390	9.92	72.27	113.93	23.02
1200	2	56.3	1170	9.60	68.34	112.68	22.15

The two data sets above were provided by M. Mahoney of Rockwell Scientific. The first set is every NAB plate for which a full set of processing parameters and material properties was gathered. The second set is comprised of the seven points which had identical tool shoulder widths (1.01 inches) and plate thickness (1.5 inches).

Each plate was processed in a raster pattern. The torque and force were measured at the beginning and end of the run. Both sets of numbers were analyzed, but the results

are nearly the same either way. For simplicity, this paper only uses the initial torque and x -direction force measurements.

The material properties listed were averaged from six tensile tests at different places on the plate. The width of the test specimen is greater than the depth of the stir zone, so the material properties are representative of the entire stir zone rather than a specific part or direction.

APPENDIX B – SIMULATION RESULTS

CTH Data							
RPM	IPM	X-dir F (kN)	X-dir Q (kW)	Rot Q (kW)	Total Q _M (kW)	Q _H	η
600	0.01	2.69	0.000	26.48	26.48	15.80	0.60
600	0.1	2.37	0.000	25.52	25.52	15.27	0.60
600	1	3.43	0.001	26.67	26.67	15.91	0.60
600	3	5.40	0.007	26.83	26.83	15.99	0.60
600	6	9.36	0.024	27.45	27.47	16.44	0.60
600	10	18.04	0.076	30.17	30.25	18.02	0.60
800	0.01	2.54	0.000	28.33	28.33	17.07	0.60
800	0.1	2.67	0.000	28.18	28.18	16.98	0.60
800	1	2.85	0.001	28.52	28.52	17.13	0.60
800	3	5.36	0.007	29.13	29.13	17.55	0.60
800	6	8.15	0.021	30.75	30.77	18.53	0.60
800	10	13.13	0.056	32.25	32.31	19.49	0.60
1000	0.01	2.63	0.000	30.34	30.34	18.23	0.60
1000	0.1	2.85	0.000	30.45	30.45	18.32	0.60
1000	1	2.92	0.001	30.51	30.51	18.34	0.60
1000	3	4.71	0.006	31.36	31.36	18.91	0.60
1000	6	7.81	0.020	32.66	32.68	19.77	0.60
1000	10	12.31	0.052	34.44	34.49	20.97	0.61
1200	0.01	2.85	0.000	32.01	32.01	19.23	0.60
1200	0.1	3.16	0.000	31.99	31.99	19.20	0.60
1200	1	3.11	0.001	32.10	32.10	19.27	0.60
1200	3	5.01	0.006	32.75	32.76	19.75	0.60
1200	6	7.38	0.019	34.18	34.20	20.74	0.61
1200	10	11.67	0.049	36.08	36.13	22.07	0.61
2000	0.01	4.16	0.000	34.83	34.83	20.87	0.60
2000	0.1	4.16	0.000	35.94	35.94	21.19	0.59
2000	1	4.36	0.002	35.29	35.29	21.10	0.60
2000	3	5.12	0.007	35.50	35.51	21.26	0.60
2000	6	7.51	0.019	37.34	37.36	22.65	0.61
2000	10	11.37	0.048	39.19	39.24	24.27	0.62

THIS PAGE INTENTIONALLY LEFT BLANK

LIST OF REFERENCES

1. W. M. Thomas et. al.: 'Friction Stir Butt Welding,' International Patent Appl. No. PCT/GB92/02203 and GB Patent Appl. No. 9125978.8, Dec 1991, U.S. Patent No. 5,460,317
2. R.S. Mishra, "Friction Stir Processing Technologies," *Advanced Materials & Processes*, v. 161, p. 43, Oct 2003.
3. C.D. Sorensen and T.W. Nelson: "Progress in Polycrystalline Cubic Boron Nitride Friction Stir Welding Process," 4th International Friction Stir Welding Symposium, Park City UT, USA, May 2003.
4. C.G. Rhodes, et al., "Effects of Friction Stir Welding on Microstructure of 7075 Aluminum," *Scripta Materialia*, v. 36, No. 1, p. 69-75, 1997.
5. R.S. Mishra and M.W. Mahoney, "Friction Stir Processing: A New Grain Refinement Technique to Achieve High Strain Rate Superplasticity in Commercial Alloys," *Materials Science Forum*, v. 357-359, p. 507-514, 2001.
6. K.V. Jata and S.L. Semiatin, "Continuous Dynamic Recrystallization During Friction Stir Welding of High Strength Aluminum Alloys," *Scripta Materialia*, v. 43, p. 743-749, 2000.
7. K. Oh-Ishi and T. McNelley, "Microstructural Modification of As-Cast NiAl Bronze by Friction Stir Processing," *Metallurgical and Materials Transactions A*, v. 35A, 2004.
8. S. Kou, Welding Metallurgy, Hoboken: Wiley, 2003.
9. R.S. Mishra, M.W. Mahoney, S.X. McFadden, N.A. Mara, and A.K. Mukherjee, "High strain rate superplasticity in a friction stir processed 7075 Al alloy," *Scripta Materialia*, v. 42, 163-168, 2000.
10. Z.Y. Ma, S.R. Sharma, R.S. Mishra, and M.W. Mahoney, "Microstructural modification of cast aluminum alloys via friction stir processing," *Material Science Forum*, v. 426-432, p. 2891, 2003.
11. American Society for Testing and Materials (ASTM) B148 – 93a, Standard Specification for Aluminum-Bronze Sand Castings.
12. M. Sahoo, "Structure and Mechanical Properties of Slow-Cooled Nickel-Aluminum Bronze Alloy C95800," *AFS Trans*, v. 90, p. 913-926, 1982.
13. P. Wenschot, "The Properties of Ni-Al Bronze Sand Cast Ship Propellers in Relation to Section Thickness," *International Shipbuilding Process*, v. 34, p. 112-123, 1987.
14. M. Sahoo, "Weldability of Nickel-Aluminum Bronze Alloy C95800," *AFS Trans*, v. 112, p. 893-911, 1982.

15. Y.J. Chao and X. Qi, "Thermal and Thermo-Mechanical Modeling of Friction Stir Welding of Aluminum Alloy 6061-T6," *Journal of Materials Processing & Manufacturing Science*, v. 7, n. 2, p. 215-233, 1998.
16. Y.J. Chao, X. Qi, and W. Tang, "Heat Transfer in Friction Stir Welding – Experimental and Numerical Studies," *Transactions of ASME*, v. 125, p. 138-145, Feb 2003.
17. M.J. Russell and H.R. Shercliff, "Analytical Modelling of Microstructure Development in Friction Stir Welding," First International Symposium on Friction Stir Welding, p. 1-11, June 1999.
18. Ø. Frigaard, Ø. Grong and O.T. Midling, "A Process Model for Friction Stir Welding of Age Hardening Aluminum Alloys," *Metalurgical and Materials Transactions A*, v. 32A, p. 1189-1200, May 2001.
19. H. Schmidt, J. Hattel, and J. Wert, "An analytical model for the heat generation in friction stir welding," *Modelling and Simulation in Materials Science and Engineering*, v. 12, 143-157, 2004.
20. P. Colegrove and H. Shercliff, "2-Dimensional CFD Modeling of Flow Round Profiled FSW Tooling," in Friction Stir Processing II, p. 13-22, TMS, Warrendale, Pennsylvania, 2003.
21. W.J. Arbogast, "Modeling Friction Stir Joining as a Metalworking Process," in Hot Deformation of Aluminum Alloys III, p. 313, TMS, Warrendale, Pennsylvania, 2003.
22. G. J. Bendzsak, T. H. North and C. B. Smith, "An Experimentally Validated 3D Model for Friction Stir Welding," The 2nd International Symposium on Friction Stir Welding, p. 1-12, Jun 2000.
23. A. Askari, S. Silling, B. London and M. Mahoney, "Modeling and Analysis of Friction Stir Welding Processes," The Minerals, Metals & Materials Society, 2001.
24. J.D. Jamison, MS Thesis, "Modeling of Thermal and Mechanical Effects During Friction Stir Processing of Nickel-Aluminum Bronze," Naval Postgraduate School, Monterey, California, June 2004.
25. J.M. McGlaun, S.L. Thompson, and M.G. Elrick, CTH: a three-dimensional shock wave physics code, *International Journal of Impact Engineering*, Vol 10 (1990) 351-360.
26. G.R. Johnson and W.H. Cook, "A constitutive model and data for metals subjected to large strains, high strain rates, and high temperatures", in Seventh International Symposium on Ballistics, The Hague, Netherlands (1983) pp 541-548.
27. S.A. Silling, "Stability and Accuracy of Differencing Methods for Viscoplastic Models in Wavecodes," *Journal of Computational Physics*, v. 104 (1993),
28. Devore, J.L., Probability and Statistics for Engineering and the Sciences, Belmont: Brooks/Cole – Thomson Learning, 2004.

29. B.K. Vasquez, MS Thesis, "The Effects of Isothermal Deformation and Annealing on the Microstructure of Nickel-Aluminum Bronze in Relation to the Friction Stir Process," Naval Postgraduate School, Monterey, CA, Dec 2002.
30. F.A. Pierce, MS Thesis, "The Isothermal Deformation on Nickel-Aluminum Bronze in Relation to Friction Stir Processing," Naval Postgraduate School, Monterey, CA, Jun 2004.
31. T. McNelley, private correspondence regarding tensile tests of hot rolled NAB at the Naval Postgraduate School, Monterey, CA, September 8th, 2005.

THIS PAGE INTENTIONALLY LEFT BLANK

INITIAL DISTRIBUTION LIST

1. Defense Technical Information Center
Ft. Belvoir, Virginia
2. Dudley Knox Library
Naval Postgraduate School
Monterey, California
3. Professor Terry McNelley
Naval Postgraduate School
Dept. of Mechanical Engineering
Monterey, California
4. Professor A. J. Healey
Naval Postgraduate School
Dept. of Mechanical Engineering
Monterey, California
5. CDR W. Plott
Naval Postgraduate School
Dept. of Mechanical Engineering
Monterey, California
6. Abe Askari
Boeing Corporation
Bellevue, Washington
7. Murray W. Mahoney
Rockwell Science Center
Thousand Oaks, California
8. William Palko
Naval Surface Warfare Center
Caderock Division
West Bethesda, Maryland
9. Dr. Leo Christodoulou
DARPA/DSO
Arlington, Virginia